European Journal of Mechanics B/Fluids 34 (2012) 19–34

Contents lists available at SciVerse ScienceDirect

European Journal of Mechanics B/Fluids

journal homepage: www.elsevier.com/locate/ejmflu

A modified High-Order Spectral method for wavemaker modeling in a numerical wave tank

Guillaume Ducrozet *, Félicien Bonnefoy, David Le Touzé, Pierre Ferrant

LUNAM Université, Ecole Centrale de Nantes, LHEEA Lab. UMR CNRS 6598 1, rue de la Noë, BP 92101, 44321 Nantes Cedex 3, France

ARTICLE INFO

Article history:
Received 14 December 2010
Received in revised form
18 July 2011
Accepted 19 January 2012
Available online 9 February 2012

Keywords:
Numerical wave tank
Nonlinear waves
High-Order Spectral
Spectral method
Directional wavemaker
Nonlinear wave generation

ABSTRACT

This paper presents the recent development on the nonlinear directional wave generation process in a 3D Numerical Wave Tank (NWT). The NWT is based on a nonlinear model using the High-Order Spectral (HOS) method, which exhibits high level of accuracy as well as efficiency properties provided by a Fast Fourier Transform (FFT) solution. The wavemaker modeling appears to be a key point in the simulation and it is carefully detailed. Different levels of approximation of the wave generation (up to third-order in nonlinearity) are studied. The properties of the numerical scheme in terms of convergence, stability and accuracy are discussed. This NWT features all the characteristics of the real wave tank (directional wavemaker, absorbing zone, perfectly reflective side walls). Furthermore, several validation results and practical applications where numerical simulations are successfully compared to experiments on 2D and 3D wave fields are presented.

1. Introduction

The safety at sea of ships and structures has always been a continuous concern of the marine hydrodynamics community. Human safety on board, environmental issues or integrity of freight and ship are the main societal concerns one has to take care of when dealing with ocean environment. These structures operate in complex nonlinear directional sea states including possible extreme events. The accurate description of these wave fields appears to be an essential need. For instance, during the design process of a ship or a marine structure, one has to describe the encountered wave patterns for fatigue studies and also to determine the design wave. Furthermore, during operations at sea, it is also essential in terms of safety or to optimize the working loads (*e.g.* oil platforms have to be stopped in rough conditions with corresponding losses ...). Consequently, the analysis of these sea states is a major concern for marine engineering and also for a better understanding of the physics of ocean waves (*e.g.* freak waves). However, the study of such complex wave fields is still very challenging either in an experimental or numerical approach.

New experimental facilities such as wave tanks have appeared in recent decades to facilitate the understanding of wave induced forces and their consequences. First, the wave fields generated in such basins can be accurately controlled and most of the characteristics of complex sea patterns can be reproduced. Second, studies on small scale models are less expensive than full scale trials, which are really difficult to set up (no control of the wave field that has to be measured for instance). This way, a wide range of experimental tests are available, from long time sea evolutions for the fatigue concern to extreme event interaction for design. Consequently, the Hydrodynamics, Energetics & Atmospheric Environment Lab. (LHEEA) of École Centrale de Nantes (ECN) built such a wave tank of size $50 \times 30 \times 5$ m, which is equipped with a 48 independent flaps wavemaker and an absorbing beach, as shown in Fig. 1.

At the same time, numerical models have been developed in the recent decades thanks to the progress of computational facilities. Many numerical tools known as Numerical Wave Tanks (NWTs) have been developed for the study of gravity waves and their propagation in a bounded domain. These constitute reliable tools to assist the set-up and analysis of experimental tests provided that they are able to accurately reproduce the 3D realistic sea patterns generated in physical wave tanks.

Different levels of approximation exist, but up until now still quite few 3D nonlinear NWTs have been developed. The study of water wave propagation without any structures can be done with the hypothesis that the fluid is non-viscous and if one furthermore assumes no wave-breaking the flow is also irrotational. Potential flow theory is therefore a correct representation of the physical phenomenon. Although attempts have been made with viscous flow formulation (for instance see [1]), the potential theory remains the best compromise for

* Corresponding author.
E-mail address: guillaume.ducrozet@ec-nantes.fr (G. Ducrozet).

0997-7546/$ – see front matter © 2012 Elsevier Masson SAS. All rights reserved.
doi:10.1016/j.euromechflu.2012.01.017

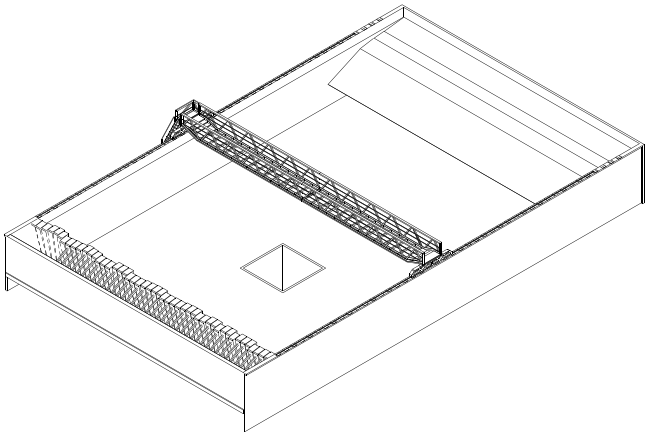

Fig. 1. ECN wave tank, 50 × 30 × 5 m.

the numerical simulation of severe sea conditions over long-time ranges. Indeed, viscous solvers are too dissipative as well as too time consuming, making them unusable in the matter of interest here. Different potential models have been developed: for example a finite element method is derived by [2] (see [3] or [4] for latest developments). In this framework, simulation tools based on Boundary Element Method (BEM) have also been elaborated allowing the simulation of overturning waves. For instance, the latest developments with High-Order BEM coupled with Fast Multipole Algorithm are applied on rogue waves generation by directional focusing in [5]. However the practical applicability is limited by the computational costs for large 3D cases where fine grids are required for the solution of a wide range of wavelengths. Fast and accurate numerical solution is required and is achieved with spectral methods, by means of Fast Fourier Transforms (FFTs). A second-order NWT based on a spectral method has been previously developed at ECN, namely *SWEET* (standing for *Spectral Wave Evolution in the* Ecn *Tank*), see [6,7]. Other methods based on spectral expansions have also shown interesting results in bounded domains (see *e.g.* [8]). A more detailed review on NWTs can be found in [9].

The SWEET model [6,7] is based on a spectral formulation. This NWT models all features of a real basin (propagation in a bounded domain, generation with a wavemaker) with the problem formulated at second-order in wave steepness and wavemaker excursion respectively. It has been extensively validated on several 2D and 3D cases and exhibits high accuracy and computational efficiency in its validity domain. The fully second-order formulation (expansion in perturbation series) limits the possible simulated steepness. The next step is thus to extend to a fully-nonlinear model this previous work. This is achieved using the High-Order Spectral (HOS) model. The initially proposed HOS method is limited to unbounded domains, modeled with periodic conditions applied on the sides of the numerical domain (see the original work of [10,11]). It therefore allows the study of open-sea evolutions once an initial sea-state has been adequately defined, the definition of this initial state being not obvious (see [12]). Moreover, in this initial HOS formulation, no wave generation is possible, making difficult experimental validations. Actually, sea evolutions reproduced in wave tanks present the additional difficulties of wall and beach reflections, generation of spurious free waves, and of starting from the rest. Nonetheless, recent developments have extended the method application range, allowing the fully-nonlinear spectral modeling of the propagation inside a wave tank. The SWEET model is thus enhanced, leading to the HOST (standing for *HOS T*ank) one, see [13]. In this HOST model, fully-nonlinear free-surface conditions have been taken into account (instead of the second-order one in SWEET) with the wavemaker still modeled at second-order. The current publication presents the latest developments of the HOST model, leading to a wavemaker modeled up to third-order, still coupled to the fully-nonlinear solution of the free surface conditions.

The present paper is divided as follows. The first part deals with the formulation of the problem in the general context of potential flow theory. The different boundary conditions are presented as well as the main characteristics of the NWT: presence of a wave-generator associated with an absorbing beach.

The second part details the numerical model. First is reported on the wavemaker modeling and particularly the improvement of the first and second-order model described in [13], which leads to the new expansion to a third-order wave generation. Then, the HOS method allowing the fully-nonlinear solution of free-surface boundary conditions is detailed. The resulting NWT characteristics in terms of efficiency and accuracy are discussed.

The third part deals with the first validation results at low steepness. Experiments have been conducted in the ECN wave basin and compared to the numerical simulations. Firstly, long time 2D irregular waves simulations are performed. The excellent agreement with experiments assess the accuracy of our NWT (wavemaker model, propagation and absorption) as well as the improvements compared to the second-order model *SWEET*. Then, the case of a 3D focused wave packet is studied. The successful comparison to experiments of this complex 3D wave pattern indicates the accuracy, efficiency and abilities of our model.

Eventually, different validations/applications at moderate steepness are presented in the last part. The case of a 2D regular wave field is analyzed with comparisons to experiments conducted in the ECN wave tank. The accuracy and efficiency is pointed out as well as the improvement obtained with enhanced wavemaker modeling. The differences between the different levels of approximation in the wavemaker modeling are analyzed. Then, the case of a 2D focused wave packet, embedded in an irregular wave field points out the possible incidence of wavemaker nonlinearities. Pressure calculations inside the fluid domain are also provided during this comparison.

2. Formulation

We consider a 3D rectangular wave tank with horizontal dimension $L_x \times L_y$ and finite depth h, filled with an homogeneous, incompressible and inviscid fluid. We choose a Cartesian coordinate system with the origin O located at one corner of the domain D. The section $x = 0$ corresponds to the wavemaker rest position, while the sections $x = L_x$, $y = 0$ and $y = L_y$ are perfectly reflective walls (see Fig. 2) and $z = 0$ is the fluid surface at rest. The notation $\mathbf{x}$ stands for the horizontal (x, y) vector.

The wave-induced motion of the fluid, initially at rest, is irrotational. Then, under these assumptions, the flow velocity $\mathbf{V} = \widetilde{\nabla}\phi(\mathbf{x}, z, t)$ derives from a velocity potential ϕ with $\widetilde{\nabla}$ standing for the 3D gradient. The continuity equation div $\mathbf{V} = 0$ is traduced for ϕ as the Laplace equation $\Delta\phi = 0$ in the fluid domain. We also assume that the waves are non-breaking and we describe the free surface elevation by a single-valued function $\eta(\mathbf{x}, t)$.

2.1. Boundary conditions

The wave tank shown in Fig. 2 contains different fixed solid boundaries which are modeled with a no-flow condition $\widetilde{\nabla}\phi \cdot \mathbf{n} = 0$ where $\mathbf{n}$ is the vector normal to the boundary. The last solid boundary ($x = 0$ section at rest) corresponds to the wavemaker, which is treated separately (see Section 2.2). Note that the wall $x = L_x$ opposite to the wavemaker is equipped with an absorbing beach whose presence is taken into account in the simulation (see Section 2.3).

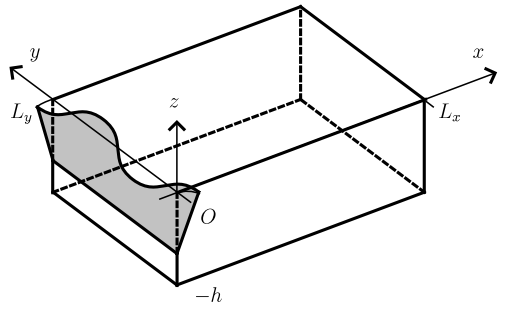

Fig. 2. Wave tank scheme with its coordinate system.

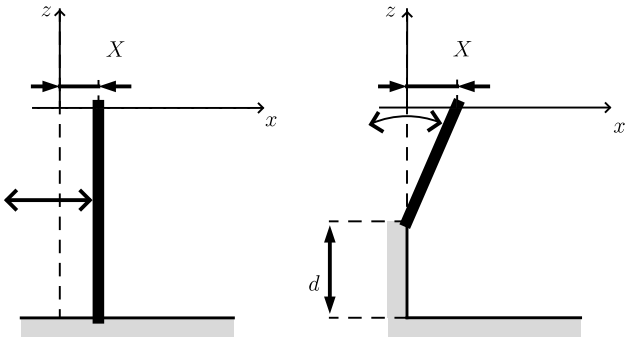

Fig. 3. Vertical geometry of piston (left) and hinged-flap (right) wavemaker.

The impermeability and the pressure continuity (surface tension is neglected) at the free surface give the kinematic and dynamic free surface boundary conditions. Following [14], these boundary conditions can be written in terms of surface quantities, namely the free-surface elevation $\eta(\mathbf{x}, t)$ and the surface potential $\phi^s(\mathbf{x}, t) = \phi(\mathbf{x}, z = \eta, t)$

$$\partial_t \eta = \left(1 + |\nabla\eta|^2\right) \partial_z \phi - \nabla\phi^s \cdot \nabla\eta \tag{1}$$

$$\partial_t \phi^s = -g\eta - \frac{1}{2}\left|\nabla\phi^s\right|^2 + \frac{1}{2}\left(1 + |\nabla\eta|^2\right)(\partial_z\phi)^2 \tag{2}$$

both expressed on the free surface location $z = \eta(\mathbf{x}, t)$. The operator ∇ stands for the horizontal gradient $\left(\partial_x, \partial_y\right)$ with ∂_x the partial derivative with respect to x. This way, the only quantity that is not explicitly defined on the free surface is the vertical velocity $W = \partial_z\phi|_{z=\eta}$, which will be evaluated thanks to the order consistent High-Order Spectral scheme of [10]. The HOS approach is detailed in Section 3.2.

2.2. Wavemaker

Following [6], the motion of the wavemaker $X(y, z, t)$ is decomposed as the product $X(y, z, t) = f_v(z)\widetilde{X}(y, t)$ where f_v is a function describing the vertical geometry. Fig. 3 shows the different types of wavemaker, piston and hinged-flap that are modeled. These are the most common wave generators used in experiments. We assume that the wavemaker is continuous in the transverse direction (*i.e.* the tiny gaps between flaps are neglected). The wavemaker condition is expressed as a no-flow condition

$$\partial_t X = \partial_x\phi - (\nabla_v X) \cdot (\nabla_v \phi) \quad \text{on } x = X(y, z, t) \tag{3}$$

with $\nabla_v = \left(\partial_y, \partial_z\right)$ the vertical gradient.

At last, note that a time ramp is superimposed to the physical wavemaker motion in order to reduce both the mechanical load and the excitation of transient long modes in the basin. This time ramp is reproduced in the numerical model as it prevents time discontinuities and helps the time stepping process. In the ECN physical wave tank, this ramp is prescribed linear and of duration 3 s. The efficiency of this ramp in the physical wave tank and NWT is discussed in [7].

The wavemaker condition Eq. (3) is derived at different levels of approximation. The previous study at first and second-order presented in [13] is extended at third-order in the present paper. This improvement in the nonlinear wave generation is presented in details in Section 3.1.

2.3. Absorbing zone

An absorbing device such as a beach is generally added on the wall opposite to the wavemaker to prevent reflection on this wall and ensure a correct wave field in the test zone. To reproduce these features in the NWT we include, following [15], an absorbing zone described by a local modification of pressure $P = \rho\nu(\mathbf{x})\widetilde{\nabla}\phi \cdot \mathbf{n}$ at the free surface, with ρ the fluid density (see [6,7] for more details).

The function $\nu(\mathbf{x})$ is non-zero where absorption is required, *i.e.* close to the wall opposite to the wavemaker. It also needs to be smooth to avoid spurious reflections at discontinuities. We found out that a third-order polynomial on a compact support satisfying $\nu = 0$ at the beginning of the numerical beach and $\partial_x\nu = 0$ at both extremities is the best choice. This function has been experimentally calibrated to reproduce the ECN absorbing zone and could be adjusted to fit any absorbing zone (see [7]).

3. Numerical model

In the following, all quantities are expressed in non-dimensional form with respect to space, time and mass scales chosen respectively as the depth h, $\sqrt{h/g}$ and ρh^3 where g is the gravity acceleration and ρ the density of the fluid.

3.1. Wavemaker modeling

The wavemaker modeling has been explained in [13] at first and second-order. This modeling is based on the approach developed for the second-order spectral model SWEET in [6]. We refer to those two papers for more details on the procedure. We recall here the key points and we present the new expansion to the third-order wave generation.

3.1.1. Additional potential

In order to model the wave generation by a wavemaker, the concept of additional potential is introduced, following [16]. We therefore separate the potential ϕ solution of the total problem into two components $\phi = \phi_{\text{spec}} + \phi_{\text{add}}$ where ϕ_{spec} is the potential describing the wave evolution in the fixed-geometry tank with its free surface (*i.e.* a homogeneous Neumann boundary condition on the wall $x = 0$), and ϕ_{add} is the additional potential accounting for the wavemaker (*i.e.* satisfying the boundary condition Eq. (3)). The free-surface boundary conditions (Eqs. (1) and (2)) are re-written with ϕ_{add} acting as a forcing term

$$\begin{cases} \partial_t\eta = \left(1 + |\nabla\eta|^2\right) W - \nabla\left(\phi^s + \phi_{\text{add}}\right) \cdot \nabla\eta + \partial_z\phi_{\text{add}} \\ \partial_t\phi^s = -\eta - \dfrac{1}{2}\left|\nabla\phi^s\right|^2 + \dfrac{1}{2}\left(1 + |\nabla\eta|^2\right) W^2 \\ \qquad - \nabla\phi^s \cdot \nabla\phi_{\text{add}} - \dfrac{1}{2}\left|\widetilde{\nabla}\phi_{\text{add}}\right|^2 - \partial_t\phi_{\text{add}} - \nu\partial_t\eta \end{cases} \tag{4}$$

on $z = \eta(\mathbf{x}, t)$ where ϕ^s and the vertical velocity W are now defined with respect to ϕ_{spec} only.

The original problem (generation and propagation of waves) is now decomposed into two subproblems with governing equations and boundary conditions reminded hereafter. First we need to find the additional potential that satisfies the wavemaker boundary condition Eq. (3) and no-flow conditions ($\partial_n\phi = 0$ with n defining

$$\phi_{\text{add}} \Rightarrow \begin{cases} \Delta\phi_{\text{add}} = 0 & \text{inside } D \\ \partial_n\phi_{\text{add}} = 0 & \text{on } x = L_x;\ y = 0,\ L_y;\ z = -1 \\ \partial_x\phi_{\text{add}} + \nabla_{\mathbf{v}}X \cdot \nabla_{\mathbf{v}}\phi_{\text{add}} = \partial_t X \partial_x\phi_{\text{spec}} - \nabla_{\mathbf{v}}X.\nabla_{\mathbf{v}}\phi_{\text{spec}} & \text{on } x = X(y, z, t) \end{cases}$$

$$\phi_{\text{spec}} \Rightarrow \begin{cases} \Delta\phi_{\text{spec}} = 0 & \text{inside } D \\ \partial_n\phi_{\text{spec}} = 0 & \text{on } x = 0, L_x;\ y = 0, L_y;\ z = -1 \\ \text{Modified free surface boundary condition: Eq. (4)} & \text{on } z = \eta(\mathbf{x}, t). \end{cases}$$

Box I.

local normal) on other boundaries. Then, we can use the free surface boundary conditions (4) to obtain the remaining unknowns, that is the second potential ϕ_{spec} (or equivalently ϕ^s) and η. This second step will be presented in details in Section 3.2. See the equations given in Box I.

The velocity potential ϕ solution of the total problem is the sum of those two potentials ($\phi = \phi_{\text{spec}} + \phi_{\text{add}}$). Therefore, it satisfies Laplace equation inside D as well as all boundary conditions.

Thus, the first challenge is to solve the additional problem, *i.e.* to determine ϕ_{add} in an efficient way. We extend here the approach presented by [13] to third-order. This approach is itself based on a NWT called *SWEET* developed by [6,7], which consists in a perturbation series at second-order. In this NWT the total problem, generation and propagation, is expanded in perturbation series up to second-order and not only the generation problem as in the present nonlinear *HOST* model. The idea is then to combine this *SWEET* model to the *HOST* formulation to have a new model featuring: (i) the *HOST* formulation, *i.e.* fully-nonlinear solution of free-surface boundary conditions and (ii) a wavemaker condition expanded up to the second or even third-order as presented in this paper. Thus, we retain the attractiveness of the *HOST* nonlinear formulation while adding an independent higher-order wave generation, which improves the accuracy of the complete NWT.

In this first step, both ϕ_{add} and ϕ_{spec} are expanded in perturbation series. In [13], we restricted the method in [6] to the successive computation of $\phi^{(1)}_{\text{add}}$, $\phi^{(1)}_{\text{spec}}$ and $\phi^{(2)}_{\text{add}}$. Note that $^{(i)}$ indicates the ith-order in perturbation series expansion of the corresponding variable and that at each order $\phi^{(i)} = \phi^{(i)}_{\text{add}} + \phi^{(i)}_{\text{spec}}$. For completeness, one reminds governing equation and boundary conditions for the problem expanded in perturbation series (see [6] for details).

$$\begin{aligned} \Delta\phi^{(i)} &= 0 && \text{inside } D \\ \partial_n\phi^{(i)} &= 0 && \text{on } x = L_x;\ y = 0, L_y;\ z = -1 \\ \partial_x\phi^{(i)} - \partial_t X^{(i)} &= A_i && \text{on } x = 0 \\ \partial_t\eta^{(i)} - \partial_z\phi^{(i)} &= B_i && \text{on } z = 0 \\ \partial_t\phi^{(i)} + \eta^{(i)} + \nu\partial_z\phi^{(i)} &= C_i && \text{on } z = 0. \end{aligned}$$

At each order the decomposition $\phi^{(i)} = \phi^{(i)}_{\text{add}} + \phi^{(i)}_{\text{spec}}$ is used for solution of the complete problem (generation and propagation). Same process than previously described in this paragraph for the nonlinear problem is used. Additional problem satisfies the wavemaker boundary condition and no-flow conditions on other solid boundaries while $\phi^{(i)}_{\text{spec}}$ takes care of free surface boundary conditions. First-order terms ($i = 1$) read

$$A_1 = 0, \qquad B_1 = 0, \qquad C_1 = 0.$$

At second-order ($i = 2$)

$$A_2 = -X^{(1)}\partial_{xx}\phi^{(1)} + \nabla_v X^{(1)}.\nabla_v\phi^{(1)}$$

$$B_2 = -\eta^{(1)}\partial_{tz}\phi^{(1)} - \frac{1}{2}\left|\tilde{\nabla}\phi^{(1)}\right|^2 - \nu\left(\eta^{(1)}\partial_{zz}\phi^{(1)} - \nabla\eta^{(1)}.\nabla\phi^{(1)}\right)$$

$$C_2 = \eta^{(1)}\partial_{zz}\phi^{(1)} - \nabla\eta^{(1)}.\nabla\phi^{(1)}.$$

Each order is solved successively up to the desired order of nonlinearity for wave generation. We are then able to evaluate the additional forcing terms in (4) using either a linear potential $\phi_{\text{add}} = \phi^{(1)}_{\text{add}}$ (model *HOST-wm1*) or a second-order potential $\phi_{\text{add}} = \phi^{(1)}_{\text{add}} + \phi^{(2)}_{\text{add}}$ (model *HOST-wm2*). Note that $\phi^{(1)}_{\text{spec}}$ was only solved to evaluate $\phi^{(2)}_{\text{add}}$ afterward. The nonlinear solution is then obtained directly from (4) and we make no use of the solution $\phi^{(1)}_{\text{spec}}$ and $\phi^{(2)}_{\text{spec}}$ of the second-order *SWEET* model in that second step.

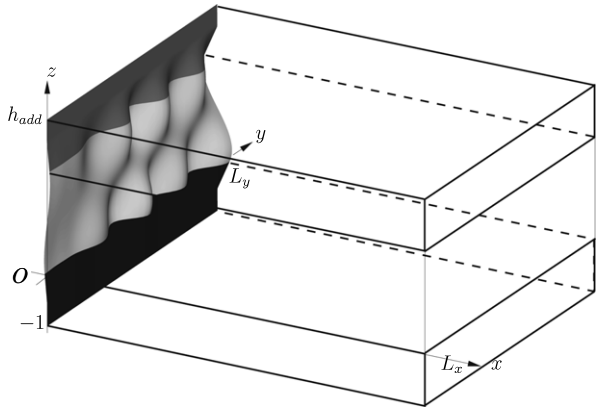

Fig. 4. Extended domain for additional problem solution.

3.1.2. *Third-order problem* HOST-wm3

We describe here the improvement of the wavemaker modeling to third-order wave generation. The wavemaker boundary condition Eq. (3) at third-order is written on $x = 0$ leading to

$$\begin{aligned} A_3 &= \partial_x\phi^{(3)}_{\text{add}} - \partial_t X^{(3)} \\ &= -X^{(2)}\partial_{xx}\phi^{(1)} - X^{(1)}\partial_{xx}\phi^{(2)} + \frac{X^{(1)^2}}{2}\partial_{xxx}\phi^{(1)} \\ &\quad + \partial_y\phi^{(2)}\partial_y X^{(1)} + \partial_y\phi^{(1)}\partial_y X^{(2)} + X^{(1)}\partial_{yx}\phi^{(1)}\partial_y X^{(1)} \\ &\quad + \partial_z\phi^{(2)}\partial_z X^{(1)} + \partial_z\phi^{(1)}\partial^{(2)}_X + X^{(1)}\partial_{zx}\phi^{(1)}\partial_z X^{(1)}. \end{aligned} \tag{5}$$

We choose to use a spectral solution for it, which enables us to use FFTs in the rectangular domain. As seen in [6], this implies to define a vertically extended domain D_{add} for solution of the additional problem. This domain is composed of

- the initial domain D extending from $z = -1$ to $z = 0$,
- the symmetrical of D with respect to $z = 0$ plan, further translated upwards between $z = h_{\text{add}} - 1$ and $z = h_{\text{add}}$,
- a matching surface between the two previous rectangular boxes, from $z = 0$ to $z = h_{\text{add}} - 1$ designed to smoothly close the domain.

Note that the wavemaker motion between $z = h_{\text{add}} - 1$ and $z = h_{\text{add}}$ is the opposite of the one from $z = -1$ to $z = 0$, in order to keep the domain volume constant when the wavemaker is moving. The size of the additional domain D_{add} is usually chosen such as $h_{\text{add}} = 3$. An example of extended domain is given on Fig. 4.

In this extended domain, we expand the additional potential ϕ_{add} as

$$\phi_{\text{add}}(\mathbf{x}, z, t) = \sum_{n=0}^{N_y}\sum_{p=0}^{N_z} B_{np}(t)\,\chi_{np}(\mathbf{x}, z) \quad \text{in } D_{\text{add}} \tag{6}$$

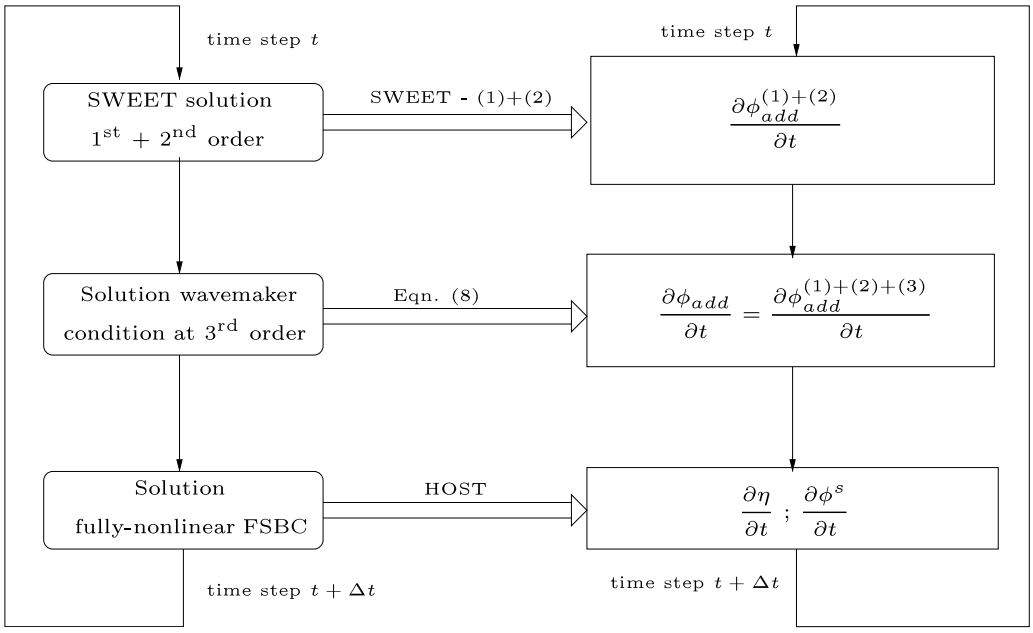

Fig. 5. Solution algorithm for model *HOST-wm3*.

with the spectral basis functions

$$\chi_{np}(\mathbf{x}, z) = \cos\left[k_n^y y\right] \cos\left[k_p^z (z+1)\right] \frac{\cosh\left[k_{np}(L_x - x)\right]}{\cosh\left[k_{np} L_x\right]} \tag{7}$$

with $k_n^y = n\pi/L_y$, $k_p^z = p\pi/(h_{\text{add}} + 1)$ and $k_{np} = \sqrt{(k_n^y)^2 + (k_p^z)^2}$.

As shown in Eq. (5), the solution of the third-order problem requires the knowledge of the total potential ($\phi = \phi_{\text{spec}} + \phi_{\text{add}}$) at lower orders. We need to determine $\phi_{\text{spec}}^{(i)}$ for $i = 1, 2$; this is achieved by means of the second-order model *SWEET*. At the same time, note that the wavemaker motion X is explicitly known. The proposed expansion in perturbation series $X^{(i)}$ is only useful to perform wavemaker corrections (for instance free waves corrections as seen in [17]).

The aim of the following section is to explain the process to obtain the time dependent amplitudes $B_{np}(t)$. We focus our attention on the more elaborated third-order scheme named *HOST-wm3* although simpler ones (*HOST-wm1* and *HOST-wm2*) were also developed [13].

3.1.3. Numerical algorithm

Eq. (4) involves the time derivative of ϕ_{add}. Instead of using backward finite difference to estimate $\partial_t \phi_{\text{add}}$, we prefer solving directly for the time derivative $\partial_t \phi_{\text{add}}$ and obtaining ϕ_{add} by means of the same time-marching scheme than that for η and ϕ^s.

The solution algorithm is schematized on Fig. 5 for the *HOST-wm3* model. It is divided into two main parts. The first one deals with the solution of the wave generation problem in the extended domain D_{add} and may be described as follows

- The first-order additional potential $\phi_{\text{add}}^{(1)}$ is time-marched after its derivative is evaluated from the linear wavemaker condition $\partial_x \phi_{\text{add}}^{(1)} = \partial_t X^{(1)}$ on $x = 0$.
- This allows the solution of the first-order free surface boundary conditions and thus the time-marching of $\eta^{(1)}$ and $\phi_{\text{spec}}^{(1)}$.
- The second-order additional potential $\phi_{\text{add}}^{(2)}$ is time-marched after its derivative is evaluated from the second-order wavemaker condition

  $\partial_x \phi_{\text{add}}^{(2)} = \partial_t X^{(2)} - X^{(1)} \partial_{xx} \phi^{(1)} + \partial_y \phi^{(1)} \partial_y X^{(1)} + \partial_z \phi^{(1)} \partial_z X^{(1)}$ on $x = 0$.
- This allows the solution of the second-order free surface boundary conditions and thus the time-marching of $\eta^{(2)}$ and $\phi_{\text{spec}}^{(2)}$.
- The third-order additional potential $\phi_{\text{add}}^{(3)}$ is time-marched after its derivative is evaluated from the third-order wavemaker condition

$$\begin{aligned}\partial_x \phi_{\text{add}}^{(3)} = {} & \partial_t X^{(3)} - X^{(2)} \partial_{xx} \phi^{(1)} - X^{(1)} \partial_{xx} \phi^{(2)} \\ & + \frac{X^{(1)^2}}{2} \partial_{xxx} \phi^{(1)} + \partial_y \phi^{(2)} \partial_y X^{(1)} + \partial_y \phi^{(1)} \partial_y X^{(2)} \\ & + X^{(1)} \partial_{yx} \phi^{(1)} \partial_y X^{(1)} + \partial_z \phi^{(2)} \partial_z X^{(1)} \\ & + \partial_z \phi^{(1)} \partial_X^{(2)} + X^{(1)} \partial_{zx} \phi^{(1)} \partial_z X^{(1)}. \end{aligned} \tag{8}$$

- The additional forcing terms in Eq. (4) assembled from $\phi_{\text{add}}^{(1)}$, $\phi_{\text{add}}^{(2)}$ and $\phi_{\text{add}}^{(3)}$.

Note that the first step is the linear wave generation used in *HOST-wm1* while the first three steps correspond to the second-order wave generation in *HOST-wm2*.

In terms of complexity of solution, one can compare the *HOST-wm3* formulation with the previous *HOST-wm1* and *HOST-wm2* ones. Several additional variables have to be time-marched: $\phi_{\text{add}}^{(3)}$, $\eta^{(2)}$ and $\phi_{\text{spec}}^{(2)}$. They have to be added to the ones already time marched in *HOST-wm1*: $\phi_{\text{add}}^{(1)}$, η, ϕ^s and *HOST-wm2*: $\phi_{\text{add}}^{(2)}$, $\eta^{(1)}$, $\phi_{\text{spec}}^{(1)}$. This results in a more computationally expensive scheme in both CPU time and memory requirement. However, this increase appears to be acceptable compared to the global CPU time (see Section 3.3.1) and regarding the corresponding improvements in the solution as shown in Sections 4 and 5.

3.2. HOS method

As mentioned in Section 3.1.1, the second step of the solution is to solve the free surface boundary conditions Eq. (4), with ϕ_{add} and $\partial_t \phi_{\text{add}}$ acting as forcing terms, in order to obtain the remaining unknowns *i.e.* the potential ϕ_{spec}, or equivalently ϕ^s, and η. This involves the estimation of the free surface vertical velocity $W = \partial_z \phi_{\text{spec}}|_{z=\eta}$. The set of Eqs. (4) then provides the time derivatives

of the unknowns η and ϕ^s, which are further used in a time-marching 4th order Runge–Kutta Cash–Karp scheme with adaptive step size [18].

Note that the perturbation technique used previously for the wavemaker modeling is abandoned here. The HOS method indeed solves for nonlinear elevation η and potential ϕ^s in Eqs. (4).

3.2.1. Principle

The HOS method is dedicated to the estimation of W. It consists in a double expansion of the potential ϕ_{spec} to solve the Dirichlet problem $\phi_{\text{spec}}(z=\eta)=\phi^s$. First the potential ϕ_{spec} is expressed as a truncated power series of components $\phi^{(m)}$ for $m=0$ to M, each component being of magnitude η^m. Second the potential taken at the free surface is expanded in a Taylor series about the mean water level $z=0$. Combining these two expansions give a triangular set of Dirichlet problems for the components that can be solved by means of a spectral method (see Section 3.2.2). Then, using the same kind of double expansion to evaluate the vertical derivative of the potential, we obtain the vertical velocity on the free surface from the components $\phi^{(m)}$.

The products involving $\nabla\eta$ and W in Eqs. (4) are evaluated thanks to the order consistent formulation of [10]. One has to keep in mind that the HOS scheme retains the fully-nonlinear feature of the solution. Indeed, the evaluation of W is an inner process, which is not correlated to the nonlinear solution of the problem (free surface boundary conditions are solved at the exact free surface position). Several validations have been performed to assess the accuracy and stability of the HOS scheme (see for instance the one reported in [19]). It is interesting to note here that the Dirichlet to Neumann Operator (DNO) models (see [20] or [21]) are strictly equivalent to the HOS model as shown in [22]. Only the formalism is different between these two methods. Furthermore, it has also been shown [23] that the HOS method (with $M=3$) is equivalent to the formalism based on the expansion of the Hamiltonian used by Zakharov [14].

3.2.2. Spectral solution

The choice of a spectral solution of the problem formulated in the previous subsection is motivated by two main features of this kind of method: (i) it allows the use of Fast Fourier Transforms (FFTs) with an efficient computational cost growing as $N\log_2 N$ and (ii) it exhibits high accuracy with quick convergence properties. The method is then intended to be more efficient than BEM models, widely used as NWT (see Introduction). However, it has to be reminded that our HOS formulation differs from this original one. Typically, spectral methods work in open domain (HOS *e.g.* [10], DNO *e.g.* [21] or mixed pseudo-spectral/integral method of [24], …) and are thus not adapted to treat the NWT issue. The spectral solution of the NWT problem is not widespread: a previous model developed in our laboratory, SWEET [6,7] was one of these. However, it was limited to second-order in wave amplitude, a limitation, which is intended to be removed with this new NWT model.

Then, the spectral expansions chosen to treat the problem of a rectangular wave tank are discussed. One has to define basis functions $\psi_{mn}(\mathbf{x},z)$, which implicitly satisfies the boundary conditions of the problem (without wavemaker, which is treated in 3.1). The potential satisfies no-flow conditions on the boundaries $x=0$ and $x=L_x$, on the side-walls $y=0$ and $y=L_y$ and on the bottom $z=-1$ as well as the Laplace equation in the domain. This gives the following basis functions, which correspond to the *natural* eigenmodes of the wave tank

$$\psi_{mn}(\mathbf{x},z)=\cos(k_m^x x)\cos(k_n^y y)\frac{\cosh\left[k_{mn}(z+1)\right]}{\cosh\left[k_{mn}\right]} \tag{9}$$

with $k_m^x=m\pi/L_x$, $k_n^y=n\pi/L_y$ and $k_{mn}=\sqrt{(k_m^x)^2+(k_n^y)^2}$. The velocity potential is expanded on this basis

$$\phi_{\text{spec}}(\mathbf{x},z,t)=\sum_{m=0}^{N_x}\sum_{n=0}^{N_y}A_{mn}(t)\psi_{mn}(\mathbf{x},z)\quad\text{in } D. \tag{10}$$

The velocity potential is fully determined by the knowledge of the time-dependent coefficients $A_{mn}(t)$.

3.3. Efficiency and accuracy

One knows that spectral solution exhibits efficient solution as well as quick convergence. This will be pointed out in next paragraphs.

3.3.1. Efficiency and computational effort

As noted before, efforts have been done in order to retain a fully spectral solution scheme (including the wave generation). This allows the use of a FFT based solution scheme. Thus, computational cost will grow as $N\log_2 N$ with N the number of modes used (either on the free surface or the wavemaker). Moreover, an improved time-marching scheme, presented by [24], is used. Thanks to an adequate change of variables, the nonlinear part of the system of Eqs. (4) is solved as a problem in itself. The linear part of the equations is solved analytically while the nonlinear part is computed numerically. This provides great speed-up of our numerical simulations as noted in [25] or [26] (total CPU time divided by a factor up to 3 for a given accuracy).

In more detail, the CPU resources needed for 3D HOS calculations are the following with a partial dealiasing of order p and denoting by $N=N_xN_y$ the number of free surface modes

$$T_{\text{HOS}_{\text{partial}}}=O\left(\left\{23+\left[\frac{M^2}{2}+\frac{7M}{2}+2E\left(\frac{M-1}{p}\right)+31\right]\frac{p+1}{2}\right\}N\log_2(N)\right). \tag{11}$$

On the other hand, the additional solution leads to an additional CPU cost that reads

$$T_{\text{add}}=O\left(\alpha N_yN_z\log_2\left[N_yN_z\right]+\beta N\log_2\left[N\right]+\gamma NN_yN_z\right) \tag{12}$$

with α, β and γ number of products/FFTs needed for additional solution/reconstruction. One can note that each operations have to be accounted for, the total CPU time being an addition of different process. To determine the different constants, this is necessary to calculate each operations performed during the computation. These are dependent of the order of approximation used in the wavemaker modeling. Results of CPU times per time-step on a 2.4 GHz Opteron mono-processor are given on Fig. 6 for a typical computation with HOS order $M=5$ and partial dealiasing $p=3$. This figure also presents the theoretical CPU time $=T_{\text{HOS}_{\text{partial}}}+T_{\text{add}}$ from Eqs. (11) and (12) with $\alpha=9$, $\beta=3$, $\gamma=48$.

The agreement between the CPU time obtained in the numerical simulation (curve *HOST-wm1*) and its approximation by Eqs. (11) *and* (12) (curve *Theoretical (wm1)*) assess the accuracy of this evaluation. Furthermore, Fig. 6 indicates the increase in CPU time when dealing with enhanced wavemaker models (*HOST-wm2* and *HOST-wm3*). The computational cost of these improvements is acceptable in the range of applications studied and particularly regarding the improvement of the results thanks to these expansions (see Section 5). Thus, the computational cost is correctly approximated by Eqs. (11) and (12) provided that the number of modes used is sufficiently large.

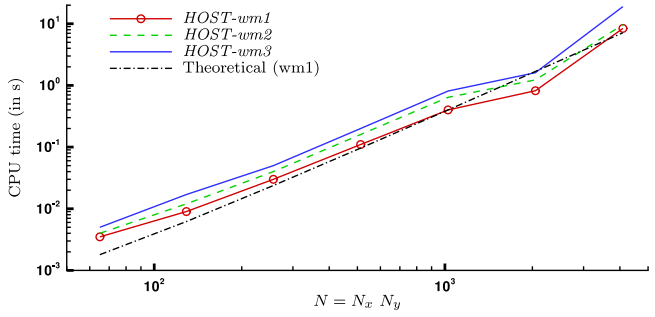

Fig. 6. Computational effort per time step function of number of modes N for first, second and third wave generation.

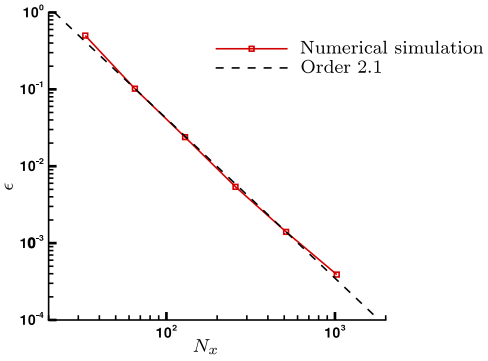

Fig. 7. Convergence of the results with respect to number of modes/points N_x.

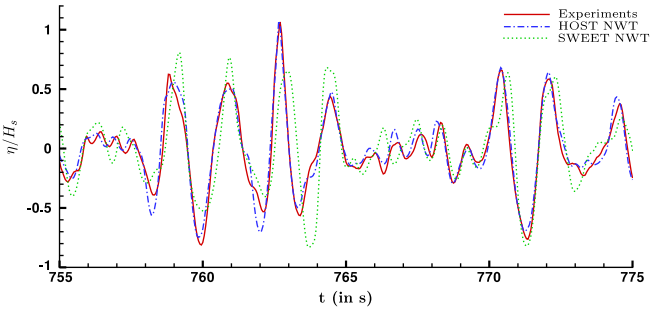

Fig. 8. Irregular-wave elevation history: comparison of experimental and NWT data for $\epsilon_c = 3\%$.

3.3.2. Accuracy

To ensure the accuracy of the solution, one has to be aware of the aliasing phenomenon, occurring in the products of two quantities in the physical space. Specific attention has been paid to treat this aliasing phenomenon correctly. Indeed, it appears to be a key point in the quality of the solution. The dealiasing is performed using the well known zero-padding approach (see *e.g.* [27]). The spectral representation of a quantity is expanded to larger modes, which are made equals to 0. Products are made with these *expanded* quantities and are then transformed back on the initial number of components/points. It has been chosen to perform a complete dealiasing, *i.e.* products of order M expressed with N modes/points are dealiased with an expansion on $\frac{M+1}{2}N$ modes/points (the $M+1$ halves rule). This enables the treatment of the complete aliasing phenomenon (by contrast with *e.g.* the approach in [11] where an expansion on only $2N$ points is always used, even with high-order products).

We also introduce the partial dealiasing as a dealiasing of the products of order $p < M$. This is applied within the HOS scheme until order M is reached. For instance, to dealiase a product of order 5 (η^5) with $p = 3$ we will rewrite ($\eta^5 = \eta^3 \times \eta^2$) and perform the dealiasing on η^3 with an expansion on $2N$ modes (here $\frac{p+1}{2} = 2$). This allows to maintain reasonable CPU time and memory storage as well as a good accuracy for large 3D computations. Thus, this partial dealiasing will be used in the following for 3D computations with $p = 3$. Typically, other computations in this paper are performed with a complete dealiasing, unless specifically provided otherwise. The influence of partial to complete dealiasing has been widely investigated in [26].

The time-stepping accuracy is achieved thanks to the 4th order Runge–Kutta Cash–Karp scheme with adaptive step size. This scheme induces the definition of a tolerance (*i.e.* a level of accuracy) on the time-marching. Time-steps are then chosen automatically during the simulation according to this tolerance which is flexible but usually fixed to 10^{-7} in the following.

A convergence analysis is proposed on a typical wave basin test case. A 2D sea state defined by a Bretschneider spectrum (peak wave length $\lambda_p = 3m$) is generated in a wave basin (50 m long, 5 m deep), and the surface elevation is recorded at one point in the middle of the NWT, which is a node for each simulation. The error ϵ is evaluated on the whole probe signal

$$\epsilon = \frac{\int_t \left|\eta_{\text{probe}} - \eta^{\text{ref}}_{\text{probe}}\right|}{\int_t \left|\eta^{\text{ref}}_{\text{probe}}\right|} \tag{13}$$

with η_{probe} the elevation at the probe signal and $\eta^{\text{ref}}_{\text{probe}}$ the probe signal of the numerical reference, corresponding to the following parameters ($N_x = 2048, N_z = 512$ vertical modes on the wavemaker, and a HOS order $M = 10$).

The results of the convergence test with respect to the number of modes/nodes in the simulations N_x are reported on Fig. 7. Results presented were performed with $N_x, N_z = N_x/4, M = 8$.

The observed convergence rate is about 2.1 and thus actually ≥ 2 as theoretically expected. With this kind of wave field the global error is less than 1% with only 128 modes/nodes in the horizontal direction to describe the 50 m long wave basin (*i.e.* $\simeq$8 modes per wavelength). That is to say, the exhibited convergence order as well as the fast solution (thanks to the use of FFTs) confirm the great efficiency of our NWT model. This efficiency enables us the crucial solution of shortest wavelengths in the NWT during 3D complex wave fields simulations. These waves are demanding in terms of discretization and are reasonably accessible (in terms of CPU time) only with very efficient numerical models. Remind that the number of modes/nodes in the computational domain depends on the wave length (for a given level of accuracy). Thus, the number used in the paper hereafter would be different if the wave conditions are changed.

4. Validations at low steepness

All experiments that are used in the following comparisons are carried out in the ECN wave basin (50 × 30 × 5 m). The geometry of the physical wavemaker is taken into account in the NWT (flap with hinge 2.15 m above the bottom). The experimental wavemaker motion serves as input for the NWT, allowing straightforward comparisons between experiments and numerical simulations.

We first propose two validations against experimental results, which do not involve strong nonlinear effects near the wavemaker. For this two cases, the three versions *HOST-wm1* to *HOST-wm3* provide elevation with only minor differences so we focus our attention on the agreement between the model *HOST-wm3* and the experiments. In depth comparisons between the three models are presented in Section 5 when steeper wave fields are generated.

4.1. 2D irregular waves: long time simulations

The first validation intends to show the ability of the model to reproduce long-time irregular wave fields in the basin. The

irregular wave field is described by a Bretschneider spectrum with a peak period $T_p = 2$ s and a steepness $\varepsilon_c = 3\%$ (the steepness is defined here as the ratio of the significant wave height $H_s = 4\sqrt{m_0}$ to the wavelength at the peak frequency). The corresponding wavemaker motion is obtained using linear wavemaker transfer function $TF = a/s$ which relates wavemaker stroke s to the generated waves amplitude a (defined here from wave spectrum).

$$X(z,t) = \mathrm{Re}\left[\sum_{j=0}^{N} TF_j a_j e^{i(\omega_j t+\varphi_j)}\right] f_v(z) \tag{14}$$

$f_v(z)$ defines the wavemaker vertical geometry (which also characterize the transfer function used). φ_j is the phase of each component j which is chosen randomly between 0 and 2π. This spectrum has been divided into 1024 frequency components equally spaced in the bandwidth [0; 2] Hz. This leads to a repeating period of 512 s for the wavemaker motion. The wavemaker is started at $t = 0$ s with a linear ramp applied during 3 s. The wave elevation is recorded at a probe located 20 m away from the wavemaker for more than 400 peak periods.

Fig. 8 compares the experimental and the HOS wave probe record for the steepness $\varepsilon_c = 3\%$. The HOS result is obtained with the *HOST-wm3* model. The time window is focused on a large wave group located at $t = 760$ s after the beginning of the experiments (*i.e.* long-time propagation, 380 T_p).

For comparisons, the same simulation is performed with the second-order NWT model named SWEET described in [6,7]. The latter NWT exhibits a high level of accuracy for a lower steepness $\varepsilon_c = 1.5\%$ even for the larger amplitude wave groups where the nonlinear effects are more pronounced (not shown here, see [7]). The probe elevation obtained with the SWEET NWT is also shown on Fig. 8.

As shown in [7], the second-order NWT SWEET is able to reproduce satisfactorily the major features of the wave field but it fails when a large amplitude wave packet is concerned, as the one between $t = 760$ and 765 s on Fig. 8. The second-order model SWEET shows both a significant phase shift and an incorrect estimation of the wave height around $t = 763$ s. This NWT does not capture the nonlinear phase velocity of the different wave components involved in the steepest wave packet.

The HOST NWT however shows a very good agreement with the experimental data during the entire time range given in Fig. 8, regardless of the local steepness. This kind of simulation shows the efficiency of the NWT to correctly: (i) generate the wave field (ii) propagate waves in the tank and (iii) model the physical wave beach for a long period of time (380 peak periods). The same absorbing zone is used in *SWEET* and *HOST* computations and its calibration is detailed in [7]. The nonlinearities of order greater than two in the propagation process are then of great influence in this kind of computation. Then, their simulations are essential when dealing with wave fields with moderate (and *a fortiori* large) steepness. The significance of our nonlinear NWT is then clear and particularly when simulations involves steep wave fields in the wave flume.

4.2. 3D focused wave packet

The second validation deals with a 3D wave packet embedded in an irregular directional wave field. The encompassing irregular wave field is described by a modified two-parameters Pierson–Moskowitz frequency spectrum with a $\cos^s\theta$ directional spreading. The experimental parameters are a 2 s peak period ($T_p = 1/f_p$), a 0.05 m significant wave height (H_s) for the frequency spectrum and $s = 20$ for the spreading.

$$S(f,\theta) = \frac{5H_s^2}{4f_p}\left(\frac{f}{f_p}\right)^5 e^{-\frac{5}{4}\left(\frac{f}{f_p}\right)^4} \cos^s\theta. \tag{15}$$

We adjust the phases φ_j of the wave components (256 in the range $f \in [0;2]$ Hz and $\theta \in [-\pi;\pi]$) in order to obtain a focus at $x_f = 24.6$ m, $y_f = 14.3$ m and $t_f = 70$ s. Spatio-temporal focusing imposes to generate each (directional) component (with angle θ_j) so that all of them are in phase at the position (x_f, y_f) at

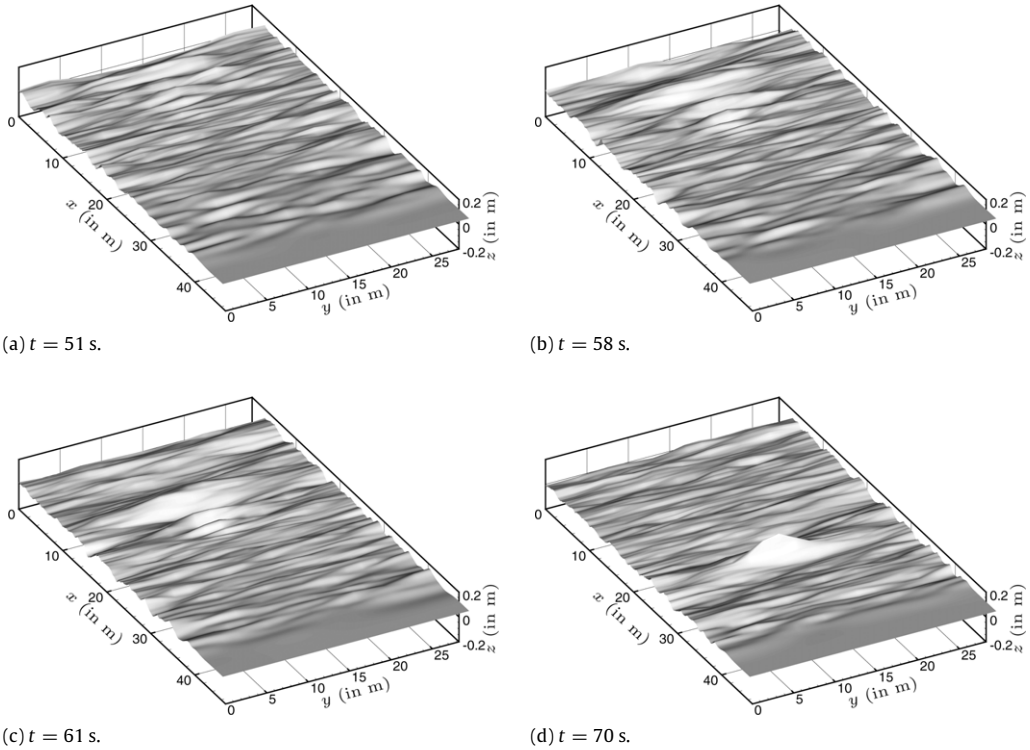

(a) $t = 51$ s. (b) $t = 58$ s.

(c) $t = 61$ s. (d) $t = 70$ s.

Fig. 9. 3D views of the focusing event.

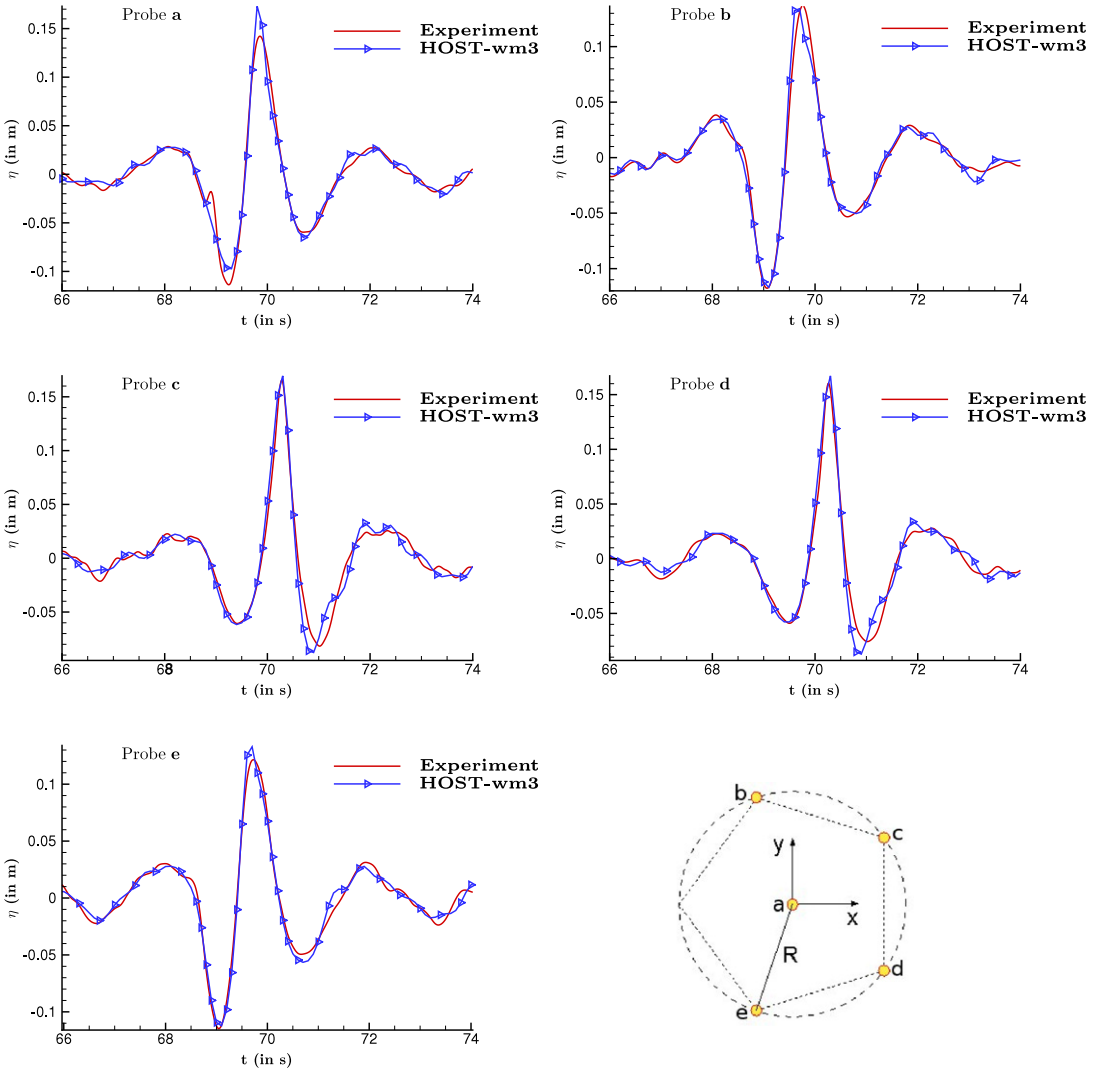

Fig. 10. Experimental and numerical results on probes surrounding the 3D focusing point.

the time t_f, *i.e.* $\varphi_j = -\left(\omega_j t_f - k_j\left[x_f \cos\theta_j + y_f \sin\theta_j\right]\right)$. This phase adjustment is based on linear dispersion relationship (to deduce wave component celerity). Then, the linear transfer function is used to deduce wavemaker motion. When dealing with directional wave fields, Dalrymple method is used to control the wavemaker instead of the more classical snake's principle. This allows to take into account the presence of reflective side walls in the wavemaker motion. We refer to [28,7] for details about the directional wavemaker theory as well as Dalrymple method. The experiments are reproduced during 90 s with *HOST-wm3* and the following numerical settings: 257 × 17 and 17 × 17 modes respectively on the free surface and wavemaker, HOS order $M = 5$ and partial dealiasing $p = 3$. The total CPU time for this simulation is around 7.5 h on a 2.4 GHz Opteron mono-processor.

Fig. 9 presents 3D views of the evolving wave field at four different instants during the focusing process. On Fig. 9(a) the wave pattern is the one of the irregular wave field generated from the directional Pierson–Moskowitz spectrum. However, the directional focusing process already started as, close to the wavemaker position ($x = 0$ m) a long wave was just generated. The typical shape of directional focusing wave fields (concentric pattern with shorter waves generated ahead of longer ones) is well observed at the consecutive instant (see Fig. 9(b) and (c)). At $t = 70$ s, the directional focusing effectively occurs with a high wave created in the middle of the wave basin, see Fig. 9(d). This wave presents a moderate local steepness $H/\lambda = 5\%$. Fig. 10 presents the wave probes signals from experiments and numerical simulations. The layout of the wave gauges, known as truncated pentagon, is also shown on this figure. This arrangement is widely used for directional wave fields studies (*e.g.* [29]). The probe **a** is located at the position of the focusing, $x = 24.6$ m, $y = 14.3$ m and the other probes are regularly spaced on a circle of 1-m radius around it.

The agreement between experiment and numerical simulation is really good at the focusing point, and on the other probes signals. The quadratic error appears to be less than 4% for all probes. This indicates that the 3D shape of the focused event is correctly reproduced as well as the surrounding troughs and crests. The superposition of different wavelengths and different directions, together with the large nonlinearities present when the wave is focusing, are correctly included within the *HOST* model, which is clearly able to model nonlinear effects in directional seas and complex 3D sea state.

5. Validations at moderate steepness

The following validations are intended to show the potential of the models *HOST-wm1*, *HOST-wm2* and *HOST-wm3*. The case of a 2D regular wave field is first studied with comparisons to experiments conducted in the ECN wave tank. The error on the

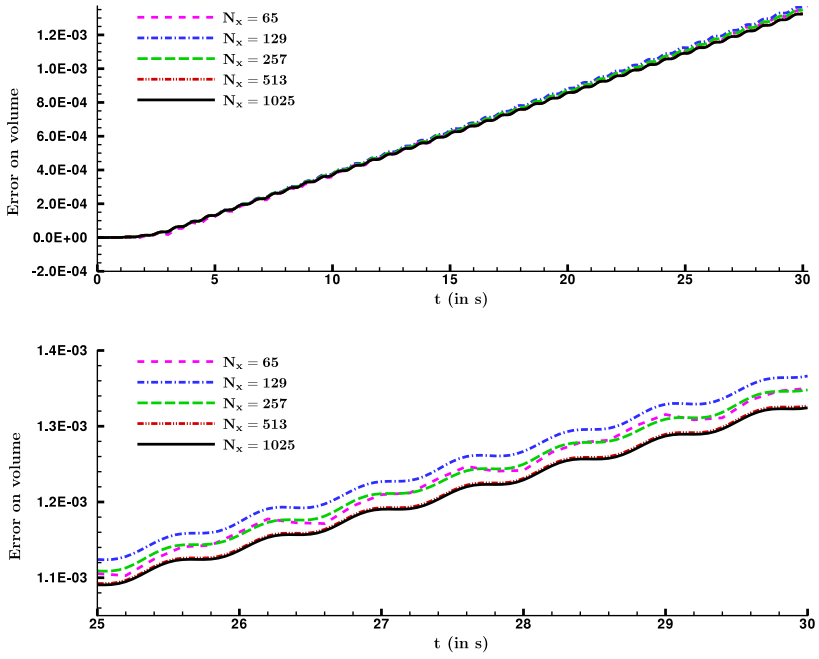

Fig. 11. Convergence on volume with respect to number of modes/points with *HOST-wm1*, $ka = 0.2$. Global view (top) and zoom on last 5 s (bottom).

free surface elevation as well as the volume conservation during simulations are analyzed. The study of the return current within the NWT is also carried on. This flow pattern is typical in bounded domains and difficult to simulate. Then, the case of a 2D focused wave packet, embedded in an irregular wave field points out the possible incidence of wavemaker nonlinearities.

5.1. 2D regular waves

The test case is regular waves propagating along the main direction of the wave basin with a moderate steepness $ka = 0.2$ and a wave period $T = 1.83$ s. The physical data consist of a single wave probe record giving the free surface elevation at a distance $x_p = 16.5$ m from the wavemaker. The wave front arrives at the probe at $t = 13$ s.

5.1.1. Volume conservation

Prior to compare the three models, we made sure that convergence in terms of Fourier modes is correct. Fig. 11 shows the relative error on the volume for this regular wave field ($ka = 0.2$) when the mesh is refined for the model *HOST-wm1*. Details on the calculation of the volume are given in Appendix A. The NWT clearly converges toward a solution where the volume increases almost linearly in time when the version *HOST-wm1* is used. In all the following simulations, we made sure that the mesh convergence is satisfied regarding the number of points in the horizontal direction as shown above but also in the vertical direction and in terms of order M and dealiasing. The numerical simulations are therefore performed in 2D with $N_x = 513$ and $N_z = 129$ modes in the x and z direction respectively and a HOS order $M = 5$ with a complete dealiasing. Fig. 12 shows the evolution of the relative error on the volume for the previous regular wave field ($ka = 0.2$) and for the three wave generation models. We can observe that the three models are characterized by an error, which is linear in time. For the worst case (*HOST-wm1*) this is less than $1.3{\cdot}10^{-3}$ after 30 s of propagation. This error is highly reduced with the second-order wave generation model *HOST-wm2* ($\simeq 1{\cdot}10^{-4}$) as well as the third-order one *HOST-wm3*, which exhibits the lowest error at the end of the simulation ($\simeq 2{\cdot}10^{-5}$).

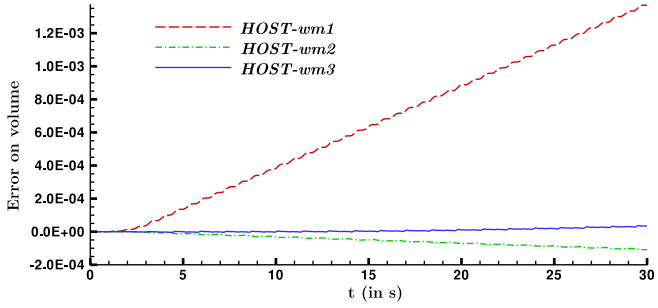

Fig. 12. Comparison between first, second and third-order generation on volume error, $ka = 0.2$. $N_x = 513$, $N_z = 65$.

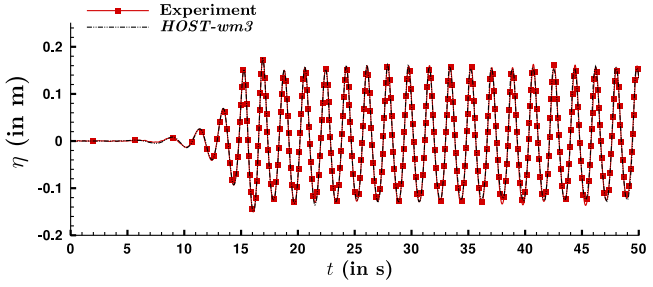

Fig. 13. Comparison between third-order wave generation and experiments for a regular wave field, $ka = 0.2$.

5.1.2. Comparison with experiments

A thorough comparison between experiment and the three *HOST-wm(i)* formulations presented previously is carried out in order to identify the physical process described by each formulation. Fig. 13 presents the wave probe signal in the physical basin and in the NWTs; the three numerical models give results that are significantly different this time, yet only the *HOST-wm(3)* is shown on Fig. 13 for clarity. One can see a correct agreement between experiment and simulation, during the transient wave front as well as during the stationary state.

To estimate the quality of the various models, we compute the global error ϵ (cf. Eq. (13)) on the wave probe record between experiment and numerical simulations. The *HOST-wm(i)* models produce 13.8%, 7.0% and 6.2% respectively for $i = 1, 2$ and 3. The solution is thus clearly improved with the enhanced wavemaker modeling.

A more in-depth analysis of the differences between models is presented below.

5.1.3. Differences between HOST-wm(1) *and* HOST-wm(2) *models*

In order to clearly identify the differences between the models of generation, we chose to apply the method used by [30] involving crest and trough wave generation. They proposed to generate two different wave fields: (i) the initial focused event η and (ii) a second focused η_π with a π phase shift for each wave components, in order to determine linear and nonlinear contributions occurring in a wave focusing. The sum and difference elevations are evaluated with

$$\eta^+ = \frac{1}{2}\left(\eta(x,t) + \eta_\pi(x,t)\right)$$
$$\eta^- = \frac{1}{2}\left(\eta(x,t) - \eta_\pi(x,t)\right).$$

To explain the meaning of these elevations, we can apply it for instance to a regular wave described at second-order by

$$\eta(x,t) = a\exp\left[i(kx-\omega t)\right] + \frac{1}{2}ka^2\exp\left[2i(kx-\omega t)\right] + O((ka)^3).$$

We obtain in this case

$$\eta^+ = \frac{1}{2}ka^2\exp\left[2i(kx-\omega t)\right] + O((ka)^3)$$
$$\eta^- = a\exp\left[i(kx-\omega t)\right] + O((ka)^3).$$

The sum elevation η^+ thus provides the second-order whereas the difference η^- the first one. In the more general context of a nonlinear elevation, which is not limited to second-order, the sum and difference elevations correspond respectively to even and odd nonlinear orders. They are evaluated with η and η_π standing now for fully-nonlinear elevations. Fig. 14 shows the difference between the even and odd elevations obtained with the first and second-order wave generation models.

The difference in sum elevation $\eta^+(\text{wm2}) - \eta^+(\text{wm1})$ identifies clearly an oscillation at frequency 2ω appearing after $\simeq$ 23 s of propagation in the *HOST-wm2* simulation. This 2ω wave propagates at the half the group velocity of the target waves: it corresponds to the spurious free wave, which is generated by nonlinear effects near the wavemaker. These waves that are also present in the physical wave basin, are reproduced numerically only with the second-order wave generation model.

For difference elevation, $\eta^-(\text{wm2}) - \eta^-(\text{wm1})$ indicates that the *HOST-wm1* and *HOST-wm2* models differ also by two components: first a ω component arriving with the wave front at $t = 13$ s, and later a 3ω component reaching the probe at $t = 30$ s. To understand the existence of such waves one can have a look to the free surface boundary conditions Eq. (4). In the case here of a second-order wave generation, the additional potential is written $\phi_{\text{add}} = \phi^{(1)}_{\text{add}} + \phi^{(2)}_{\text{add}}$ and it gives the following terms in the dynamic boundary condition

- $\partial_t\phi^{(2)}_{\text{add}}$ is related to the free waves of pulsation 2ω propagating with a group velocity half that of the ω waves.
- $|\tilde{\nabla}\phi^{(1+2)}_{\text{add}}|^2$ gives a term $|\tilde{\nabla}\phi^{(1)}_{\text{add}}.\tilde{\nabla}\phi^{(2)}_{\text{add}}|$ including ω and 3ω components, which appear clearly in bottom part of Fig. 14.
- $\nabla\phi^s \cdot \nabla\phi^{(1+2)}_{\text{add}}$: results also in ω and 3ω components.

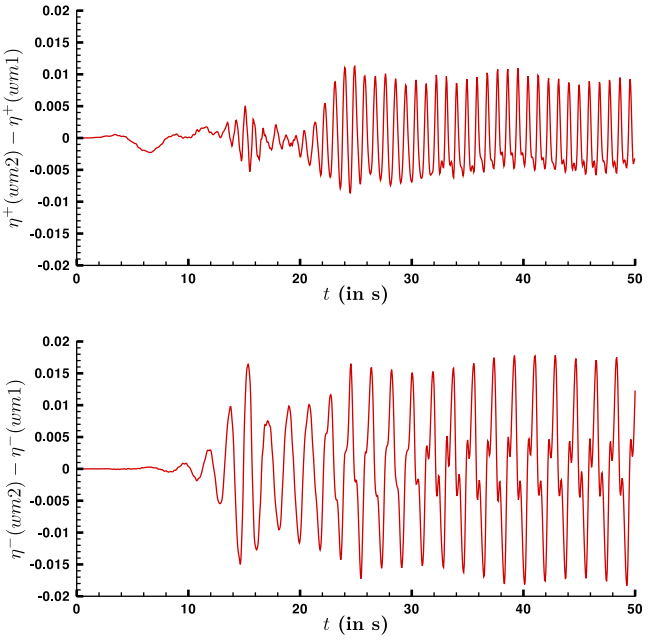

Fig. 14. Differences between first and second-order wave generation using even (top) and odd (bottom) elevation for a regular wave field, $ka = 0.2$.

The ω component in $\eta^-(\text{wm2}) - \eta^-(\text{wm1})$ proves that third-order effects such as the one mentioned above contribute to the amplitude of the propagating wave field. The 3ω component arrives later: it corresponds to a free wave also generated by nonlinear effects near the wavemaker.

5.1.4. Differences between HOST-wm(2) *and* HOST-wm(3) *models*

Fig. 15 presents the difference of the odd and even elevations between *HOST-wm2* and *HOST-wm3*. A comparison of the latter with Fig. 14 shows that the process of increasing the order of the wave generation model is indeed converging, more or less rapidly depending on the nature of the waves involved. One may first observe that the amplitude of the difference between the odd elevation is globally lower than in the previous *HOST-wm1* and *HOST-wm2* case (bottom). This means that the other third terms in Eq. (4) also significantly contribute to the total ω amplitude in the wave field. Concerning the even elevation (top) we see that the models *HOST-wm2* and *HOST-wm3* give the same results before $t = 23$ s but not after. The second-order wave generation model is able to reproduce the even nonlinearities before the spurious 2ω wave field arrives but fails once the latter reaches the probe: in this case, the third-order wave generation is required.

5.1.5. Return current

The well known Stokes drift describes a mass transport in the waves direction. This will result, in confined domain such as a wave basin, in the existence of a return current to compensate for the Stokes drift. If we assume a constant velocity profile with depth, the second-order theory of water waves gives the return current (period averaged and averaged over the still water depth—see *e.g.* [31,32])

$$U_r = -\frac{1}{2}\frac{A^2\omega}{h}\coth(kh). \tag{16}$$

Fig. 16 presents, on the top part, the current estimated in the simulations with the three methods of wave generation *HOST-wm1*, *HOST-wm2* and *HOST-wm3*. This current is measured at the bottom of the wave basin ($h = -5$ m) where the wave flow influence is negligible. The velocity calculation is performed at

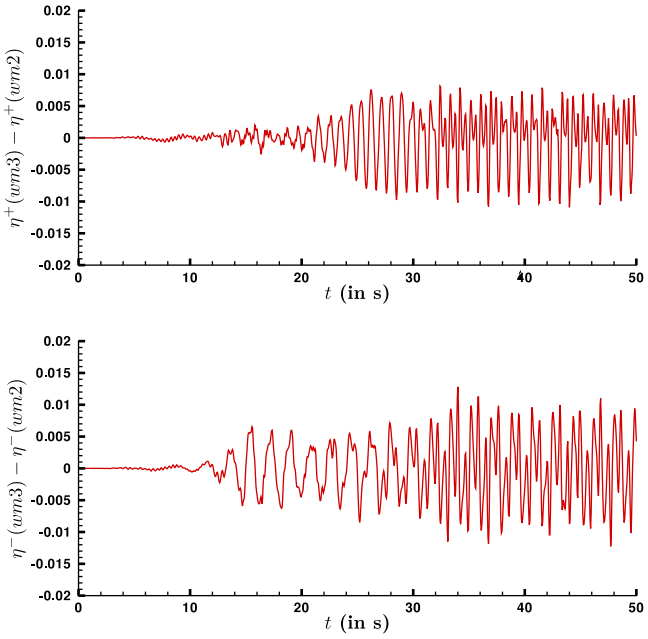

Fig. 15. Differences between second and third-order wave generation using even (top) and odd (bottom) elevation for a regular wave field, $ka = 0.2$.

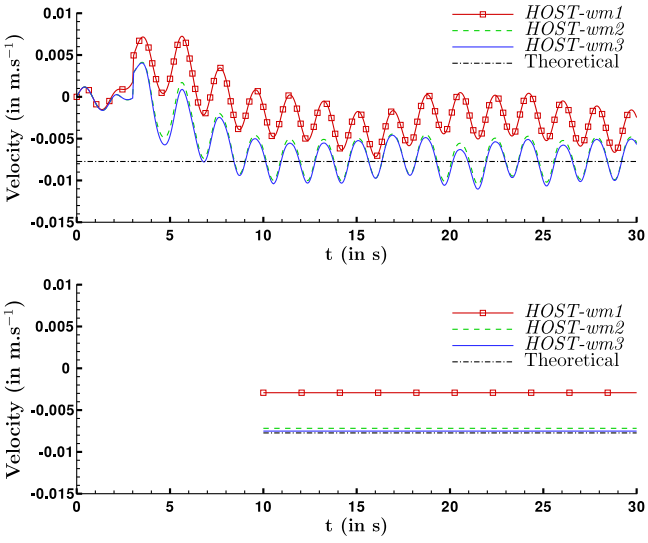

Fig. 16. Velocity on bottom during time: *HOST-wm1*, *HOST-wm2*, *HOST-wm3* and theoretical with $ka = 0.2$. Exact velocity (top) and mean value (bottom).

$x = 7$ m and one can note that as shown in [33], the return current is traveling with the wave front (at $t = 10$ s the wave field reaches the location of the velocity probe). After the wave front, the second-order current presents a mean value, the so-called 'return current', and an oscillating part at twice the wave frequency. The mean value is shown on the bottom part of Fig. 16. It appears that the *HOST-wm2* and *HOST-wm3* computations are in good agreement with this theoretical result (Eq. (16)), the error being drastically reduced from first to second-order wave generation. The third-order one is, as expected, the most accurate with very slight discrepancy with the theory. Furthermore, this small difference between numerical simulations and the 'theoretical' model could maybe be explained by the approximation of second-order water waves as well as a constant velocity profile with depth. However, the discrepancies observed with the *HOST-wm1* model are due to the strong hypothesis of a first-order wavemaker and more precisely, are mainly due to the volume drift observed previously. Indeed, a change of global volume could be seen as a non-null flow rate through a given water column and thus resulting in a change of the return current (which ensure the global mass conservation inside the wave basin). Thus, it appears that some complex phenomena could only be correctly modeled with the high-order (second or third) wave generation. The relevance of the improved wavemaker modeling is clear. It is to be noted that the interesting feature of the return current in a 3D wave basin (*i.e.* with 3D wave sea patterns) can be easily analyzed with our method.

5.2. Limitations

During the development of this enhanced wavemaker models, we observed few limitations. Particularly, when one tries to simulate the propagation of steep waves ($ka = 0.3$ and larger), some problems occur during the solution with the *HOST-wm3* model. Sawtooth instabilities appear in the additional solution, which do not allow a correct simulation. As far as spectral methods are concerned, this kind of instability may be typical of aliasing. However all the products are evaluated using an alias-free scheme (see Section 3.3.2) so the instability is more likely related to the wave generation process (additional problem) rather than wave propagation (HOS method).

To analyze the origin of such instabilities, one has to look at the wavemaker boundary conditions at third-order Eq. (8). This condition implies the computation of the third-order spatial derivative of the first-order velocity potential $\partial_{xxx}\phi^{(1)}$ and the second-order spatial derivative of the second-order velocity potential $\partial_{xx}\phi^{(2)}$. These derivations are performed in the Fourier domain and they could induce some stability problems: the successive derivations increase the numerical errors, particularly for larger modes (multiplication by k^3 or k^2). Indeed, the behavior of Fourier components at large wavenumbers depends on the regularity of the function. We may investigate separately the additional potential ϕ_{add} and the remaining component ϕ_{spec}.

To guarantee first the regularity of the additional potential at the different orders we have removed two sources of discontinuity. As seen in Section 3.1 a matching surface is determined to build the additional domain where the additional problem is solved. This surface is chosen with continuous derivatives up to the third-order to ensure the regularity of the different derivatives further needed in the numerical computation. Furthermore, a discontinuity of $\phi^{(1)}_{\text{add}}$ appears at the bottom of the flap (rotation axis) in the case of a hinged-flap wavemaker (typically used in wave basins). This singularity is removed smoothing locally around the hinge the vertical geometry of the flap, in order to obtain an additional potential whose derivatives are continuous up to the third-order. This is obtained thanks to a 6th order polynomial in a small smoothing zone around the hinge. Once this is done, the Fourier components of $\phi^{(1)}_{\text{add}}$ decrease faster than k^{-4}, which ensures a correct spatial derivation. It also follows that the second-order additional potential is twice derivable.

The second step is to study the second component of the potential, *i.e.* the potential ϕ_{spec}. Particularly, the wavemaking process involves $\partial_{xxx}\phi^{(1)}_{\text{spec}}$ as well as $\partial_{xx}\phi^{(2)}_{\text{spec}}$ at the position of the wavemaker ($x = 0$). The first term involving the third derivative in x of a quantity will be equal to 0: we recall that the spectral expansions of the different quantities (including $\phi^{(i)}_{\text{spec}}$) involve cosinus series, Eqs. (9) and (10). Studying the behavior of $\partial_{xx}\phi^{(2)}_{\text{spec}}$ informs us that the decrease of its Fourier series components is around k^{-2} for the steep cases, which induce the problematic sawtooth instabilities. Thus, for these wave fields, the regularity of this function is not sufficient to provide with good accuracy its second-order spatial derivative (multiplication by k^2) and

consequently the third-order wave generation is not resolved properly. This feature is mainly due to the way $\phi^{(2)}_{\text{spec}}$ is obtained during the SWEET solution process. Indeed, its computation involve several derivatives of the first-order quantities, which results in a lower convergence rate for this quantity. To overcome this difficulty, one can think about applying some kind of filtering for instance but up until now, no satisfactory scheme have been obtained for the treatment of very steep wave fields with *HOST-wm3* model.

5.3. Focused waves

The next step in validation is to consider a transient wave field with a full range of frequencies and not only a single frequency as for the regular wave previously studied. We test the NWT for the generation of a focused wave packet where the nonlinear effects consist of more complex wave–wave interactions. A set of experiments has been conducted in the ECN wave tank with the following superposition of 2 wave fields (2D):

- Irregular wave field defined by a Bretschneider spectrum $H_s = \alpha$ 0.5 m and $T_p = 3.13$ s.
- Focused wave packed defined by a Bretschneider spectrum $H_s = \alpha$ 0.075 m and $T_p = 3.13$ s with phases adjusted to produce a focusing at the specified position.

As seen previously, wavemaker motion is obtained for each wave field from Eq. (14) before the superposition. 512 wave components are used to describe each spectrum in the range $f \in [0; 2]$ Hz. Random phases (between 0 and 2π) are used for the first one while they are adjusted to have focusing at a distance $x_f = 16.1$ m from the wavemaker at $t_f = 17$ s for the second one. The above spectra parameters have been tuned experimentally to provide a wave field suitable to study the survivability of a wave energy converter device. The case $\alpha = 1$ is the steepest wave field we could possibly generate without having wave breaking between the wavemaker and the probes location. With this set-up, the wave breaks just after the wave probes.

The numerical simulations are performed with $N_x = 513$ modes on the free surface and $N_z = 129$ modes on the wavemaker. The HOS order is fixed to $M = 5$ with a complete dealiasing and the duration of the simulation is $t = 30$ s real time (when no wave-breaking occur) for a total CPU time of around 450 s on a 2.4 GHz Opteron mono-processor (*HOST-wm3*).

As noted in Section 5.2, for highly nonlinear sea states some stability problems could occur. This is the case for the steepest wave fields described above. Then, we put our interest here only on the cases $\alpha = [0.5; 0.6; 0.7]$ for the comparisons between the different *HOST-wm(i)* models. The cases with $\alpha = [0.8; 0.9; 1.0]$ have already been successfully simulated with *HOST-wm1* and *HOST-wm2* models (see [13]). Note that the simulation of irregular seas possibly include highly nonlinear waves. Indeed, those events are usually localized in space and time in this configuration. Consequently, numerical instabilities observed with regular waves are greatly reduced, allowing simulation of those complex nonlinear wave fields.

5.3.1. Surface elevation

In order to assess the higher accuracy of the *HOST-wm3* model, the 3 models of generation are used on the cases $\alpha = [0.5; 0.6; 0.7]$ and compared to the experiments. The simulations are 30 s long and no wave breaking occurs here. Fig. 17 presents the comparison between experimental results and numerical simulations with the three models of generation for $\alpha = 0.7$. One can see that experiments and numerical simulations are in good agreement for the three models (top). The bottom part of Fig. 17 presents a closer view of the focused event and it reveals

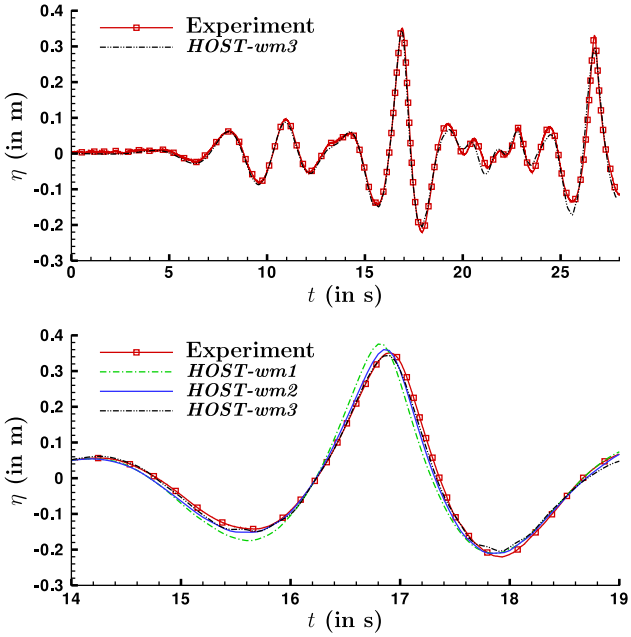

Fig. 17. Comparison between first, second and third-order generation and experiments ($\alpha = 0.7$).

Table 1
Global error ϵ with respect to wavemaker modeling for different choices of α.

	HOST-wm1 (%)	*HOST-wm2* (%)	*HOST-wm3* (%)
$\alpha = 0.5$	13.7	9.8	8.2
$\alpha = 0.6$	14.6	10.1	7.4
$\alpha = 0.7$	18.8	13.7	9.5

that the *HOST-wm1* model fails to accurately reproduce this event, more specifically the trough preceding the focused crest and this crest itself. The higher-order generation models allows to correct the errors observed with the linear one. In order to quantify the improvement of the higher-order models, Table 1 presents the global error on the wave elevation (Eq. (13)) evaluated over the 30 s simulation with the three models of wave generation. The cases $\alpha = [0.5; 0.6; 0.7]$ are listed. The first point to note is that the error in Table 1 increases with the wave amplitude α, that is to say, with nonlinearities. We can also see that both *HOST-wm2* and *HOST-wm3* models present real improvements compared to *HOST-wm1*. The *HOST-wm3* model is in this study still, as expected, the most accurate model.

As most of the nonlinear effects are correctly solved by the *HOST-wm2* model and as this model does not suffer the stability problems encountered with the *HOST-wm3*, it seems to be a good compromise between accuracy/stability and solution efficiency.

5.3.2. Pressure calculations

In this section, we focus our attention on the calculation of the pressure under the free surface. The experimental set up of the focused wave presented before also provide pressure gauges. The case of interest here is $\alpha = 0.7$ and the numerical simulations are performed with the *HOST-wm3* model.

As regards the numerical evaluation of the pressure inside the fluid domain, a specific technique is implemented in our model; it is adapted from a previous work by [34] who developed the so-called H and H_2 operators in a DNO method (which is equivalent in its accelerated version to the HOS scheme). Further details on these underwater velocity/pressure calculation can be found in [25] where it has especially been demonstrated that: the best way of calculating the underwater kinematics (and thus the pressure)

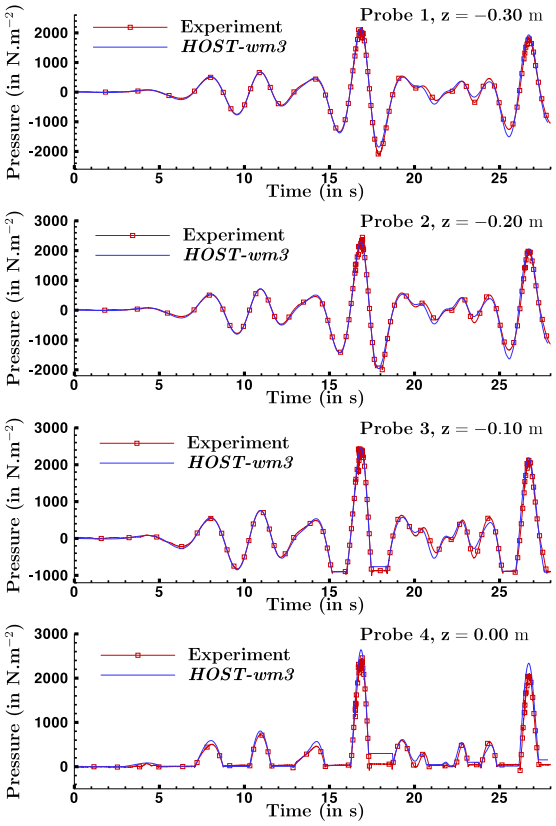

Fig. 18. Comparison of pressure under the free surface between numerical simulations *HOST-wm3* and experiments.

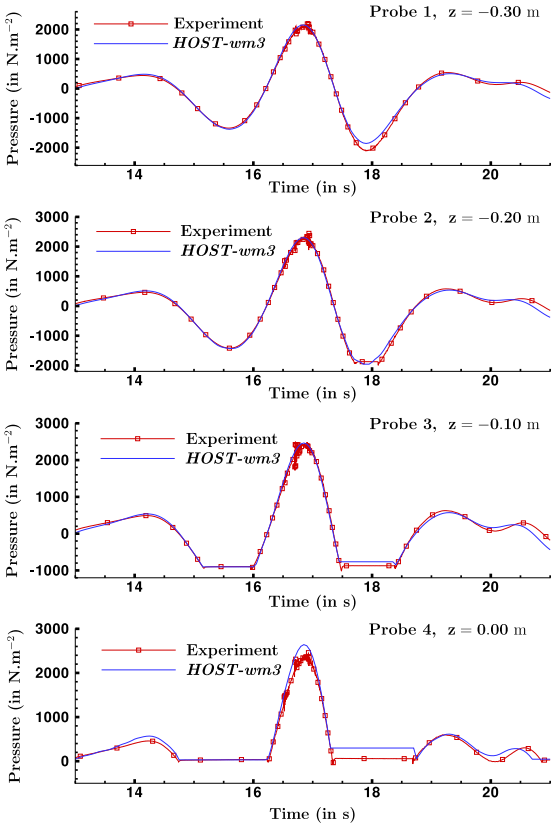

Fig. 19. Zoom of Fig. 18, comparison of pressure between numerical simulations *HOST-wm3* and experiments.

is to take as initial value the corresponding velocity at the free surface and not the surface velocity potential. Furthermore, the H_2 operator has been found substantially more accurate than the H one with steep waves.

The comparisons are achieved on the pressure gauges signals located at the focusing position and at different depths ($z = -0.30$, -0.20, -0.10 et 0.00 m). Results are presented on Fig. 18 and note that the y-axis denotes the dynamic pressure of the flow.

Firstly, one can note in this figure some flat parts in the temporal signals. These corresponds to the time periods where the pressure sensors are outside the fluid. In the calculations, one assumed the pressure to have a constant value during these excursions outside the fluid for easier comparison between experiments and numerical simulations. Note that the small errors observed on the level of these flat parts are mainly due to a little phase-shift between experiments and numerical simulations. This induces that the moment of the beginning of the excursion is not perfectly reproduced and consequently that one has an incorrect level for the whole flat part. Otherwise, the numerical simulations are in excellent agreement for each probe during the whole experiment. A zoom on the more demonstrative part (focused wave formation) is reported in Fig. 19.

The accuracy of the simulation of this highly nonlinear phenomenon is confirmed. Little discrepancies exist and particularly on the probe signal located at $z = 0$ m. This is due to the numerical operator H_2 used to compute this pressure, which tends to amplify numerical errors close to the free surface. However, the numerical simulations have still good accuracy compared to experiments.

These comparisons demonstrates again the capabilities of our model, able to accurately reproduce not only the kinematics of the evolution in the wave tank but also the free-surface and underwater dynamics.

6. Conclusion

In the present paper, the development of an efficient and accurate 3D NWT is presented. It is based on a nonlinear HOS scheme, which exhibits attractive numerical characteristics such as a fast solution with FFTs coupled to an accelerated scheme, and a fast convergence providing high accuracy when the nonlinear products involved are carefully dealiased. This numerical model was initially applied to unbounded domain and recent developments have extended the method application range to the modeling of a wave tank including all its features: directional wavemaker, absorbing zone, perfectly reflective side walls.

The HOST method and its numerical properties have been detailed and more particularly the wavemaker modeling, which appears to be a key point in the simulation, is detailed. The concept of additional potential is introduced allowing a spectral solution of the wavemaking problem. The new expansion to the third-order wave generation based on the improvement of the first and second-order model described previously in [13] is detailed. This leads to a new NWT, namely *HOST-wm3* whose characteristics in terms of efficiency and accuracy are investigated.

Firstly, validations with low steepness cases have been carried out to assess the accuracy of the solution. In the first place, long-time 2D irregular waves are studied. The successful comparisons emphasize the ability of the numerical model to: (i) correctly generate the wave field (ii) accurately propagate waves in the tank and (iii) satisfactorily model the physical absorbing beach. Furthermore the improvements of our fully-nonlinear NWT compared to a second-order one are discussed.

Secondly, the complex case of a 3D directional focusing event embedded inside a 3D irregular wave field is studied. We provide convincing comparisons between the *HOST-wm3* model and experiments on different wave probes signals measured around

the focusing point. The accurate simulation of this 3D focused event indicates the ability of the model to deal with complex 3D sea states and thus to reproduce any experiments conducted in a rectangular wave tank (with the exception of breaking waves).

The last part presents different validations/applications with wave fields at moderate steepness. Firstly, the case of 2D regular waves ($ka = 0.2$) is presented. Some experiments have been conducted in the ECN wave basin and comparisons on a wave probe signal indicate the accuracy of our *HOST* models. The improvements of the second and third-order wave generation are established compared to the first-order one and are investigated in details. The advanced wavemaker modeling allows more accurate simulations and particularly allow to take into account the different physical processes involved during the wave generation (*e.g.* generation of free waves). The volume conservation during numerical simulations is also studied, confirming the improvements observed with the advanced wavemaker modeling. These appear also clearly during the study of the return current inside the wave tank. However, stability issues with the third-order model are reported on at large steepness, limiting its range of application. Note that it has been found previously [13] that the second-order wave model is still accurate at large steepness.

The necessity of such an advanced model to precisely reproduce all the physical features occurring in a wave tank is then clear. In the end, the case of a 2D focused wave packet embedded in an irregular wave field is analyzed. This kind of sea pattern involves a wide range of wavemaker motions and nonlinearities. This test case is thus suitable for the study of the improved wavemaker modeling and the excellent agreement obtained between *HOST-wm3* and experiments confirms the accuracy of our method.

Appendix. Volume calculation

Here is explained the method used to compute the 2D volume $\mathcal{V}$ inside the fluid domain D. One recalls that the depth is in non dimensional form $h = 1$

$$\mathcal{V}(t) = \int_D d\mathcal{V} = \int_{X(z,t)}^{L} \int_{-1}^{\eta(x,t)} dxdz. \tag{A.1}$$

The volume is split in different parts

$$\begin{aligned}
\mathcal{V}(t) &= \int_{X(z,t)}^{0} \int_{-1}^{\eta(x,t)} dxdz + \int_{0}^{L} \int_{-1}^{\eta(x,t)} dxdz \\
&= \int_{X(z,t)}^{0} \int_{-1}^{0} dxdz + \int_{X(z,t)}^{0} \int_{0}^{\eta(x,t)} dxdz \\
&\quad + \int_{0}^{L} \int_{-1}^{0} dxdz + \int_{0}^{L} \int_{-1}^{\eta(x,t)} dxdz \\
&= \int_{-1}^{0} X(z,t)dz + \int_{X(z,t)}^{0} \int_{0}^{\eta(x,t)} dxdz + L + \int_{0}^{L} \eta(x,t)dx \\
&= L + \int_{0}^{L} \eta(x,t)dx + \int_{-1}^{0} X(z,t)dz + \int_{X(z,t)}^{0} \int_{0}^{\eta(x,t)} dxdz \\
&= \mathcal{V}_{\text{rest}} + \mathcal{V}_{\text{SL}} + \mathcal{V}_{\text{wmk}} + \mathcal{V}_{\text{int.}}
\end{aligned} \tag{A.2}$$

with $\mathcal{V}_{\text{rest}} = L$ the volume of the wave basin at rest, $\mathcal{V}_{\text{FS}} = \int_0^L \eta(x,t)dx$ the volume of the free surface (without wavemaker), $\mathcal{V}_{\text{wmk}} = \int_{-1}^{0} X(z,t)dz$ the one due to the presence of the wavemaker (without free surface elevation) and finally $\mathcal{V}_{\text{int.}} = \int_{X(z,t)}^{0} \int_{0}^{\eta(x,t)} dxdz$ the correction to take into account the simultaneous presence of the wavemaker and the free surface.

Computation of $\mathcal{V}_{\text{rest}}$, $\mathcal{V}_{\text{FS}}$ et $\mathcal{V}_{\text{wmk}}$ is straightforward, only $\mathcal{V}_{\text{int.}}$ as to be approximated

$$\mathcal{V}_{\text{int.}} \simeq X(0,t)\,\eta(0,t) \tag{A.3}$$

one refers to [35] for more details on volume calculations and particularly to assess that this computation of $\mathcal{V}_{\text{int.}}$ is precise up to second-order.

References

[1] J.C. Park, M.H. Kim, H. Miyata, H.H. Chun, Fully nonlinear numerical wave tank (NWT) simulations and wave run-up prediction around 3D structures, Ocean Eng. 30 (2003) 1969–1996.

[2] G. Wu, Q. Ma, R.E. Taylor, Numerical simulation of sloshing waves in a 3D tank based on a finite element method, Appl. Ocean Res. 20 (1998) 337–355.

[3] Q.W. Ma, S. Yan, QALE-FEM for numerical modelling of non-linear interaction between 3D moored floating bodies and steep waves, Internat. J. Numer. Methods Engrg. 78 (2009) 713–756.

[4] S. Yan, Q.W. Ma, QALE-FEM for modelling 3D overturning waves, Internat. J. Numer. Methods Fluids 63 (2010) 743–768.

[5] C. Fochesato, S. Grilli, F. Dias, Numerical modeling of extreme rogue waves generated by directional energy focusing, Wave Motion 44 (2007) 395–416.

[6] F. Bonnefoy, D. Le Touzé, P. Ferrant, A fully-spectral time-domain model for second-order simulation of wavetank experiments. Part A: formulation, implementation and numerical properties, Appl. Ocean Res. 28 (2006) 33–43.

[7] F. Bonnefoy, D. Le Touzé, P. Ferrant, A fully-spectral time-domain model for second-order simulation of wavetank experiments. Part B: validation, calibration versus experiments and sample applications, Appl. Ocean Res. 28 (2006) 121–132.

[8] M. Chern, A. Borthwick, R.E. Taylor, A pseudospectral σ transformation model of 2D nonlinear waves, J. Fluids Struct. 13 (1999) 607–630.

[9] C. Kim, A. Clément, K. Tanizawa, Recent research and development of numerical wave tanks—a review, Int. J. Offshore Polar Eng. 9 (1999) 241–256.

[10] B. West, K. Brueckner, R. Janda, M. Milder, R. Milton, A new numerical method for surface hydrodynamics, J. Geophys. Res. 92 (1987) 11803–11824.

[11] D. Dommermuth, D. Yue, A high-order spectral method for the study of nonlinear gravity waves, J. Fluid Mech. 184 (1987) 267–288.

[12] D. Dommermuth, The initialization of nonlinear waves using an adjustment scheme, Wave Motion 32 (2000) 307–317.

[13] G. Ducrozet, F. Bonnefoy, D. Le Touzé, P. Ferrant, Implementation and validation of nonlinear wave maker models in a HOS numerical wave tank, Int. J. Offshore Polar Eng. 16 (2006) 161–167.

[14] V. Zakharov, Stability of periodic waves of finite amplitude on the surface of a deep fluid, J. Appl. Mech. Tech. Phys. (1968) 190–194.

[15] J.-H. Westhuis, The numerical simulation of nonlinear waves in a hydrodynamic model test basin, Ph.D. Thesis, Universiteit Twente—MARIN, Twente, The Netherlands, 2001.

[16] Y. Agnon, H.B. Bingham, A non-periodic spectral method with applications to nonlinear water waves, Eur. J. Mech. B Fluids 18 (1999) 527–534.

[17] F. Bonnefoy, D. Le Touzé, P. Ferrant, Génération de houle directionnelle au second ordre: prédiction et contrôle des ondes libres, in: Proc. 16ème Congrès Francais de Mécanique (in French).

[18] J.R. Cash, A.H. Karp, A variable order Runge–Kutta method for initial value problems with rapidly varying right-hand sides, ACM Trans. Math. Software 16 (1990).

[19] F. Bonnefoy, G. Ducrozet, D. Le Touzé, P. Ferrant, Time-domain simulation of nonlinear water waves using spectral methods, in: Qingwei Ma (Ed.), Advances in Numerical Simulation of Nonlinear Water Waves, The World Scientific Publishing Co., 2010, (Chapter 4).

[20] W. Craig, C. Sulem, Numerical simulation of gravity waves, J. Comput. Phys. 108 (1993) 73–83.

[21] W. Bateman, C. Swan, P. Taylor, On the efficient numerical simulation of directionnally-spread surface water waves, J. Comput. Phys. 174 (2001) 277–305.

[22] H. Schäffer, Comparison of Dirichlet–Neumann operator expansions for nonlinear surface gravity waves, Coastal Eng. 55 (2008) 288–294.

[23] M. Onorato, A. Osborne, M. Serio, On the relation between two numerical methods for the computation of random surface gravity waves, Eur. J. Mech. B Fluids 26 (2007) 43–48.

[24] D. Fructus, D. Clamond, J. Grue, O. Kristiansen, An efficient model for three-dimensional surface wave simulations. Part I: free space problems, J. Comput. Phys. 205 (2005) 665–685.

[25] G. Ducrozet, F. Bonnefoy, D. Le Touzé, P. Ferrant, Development of a fully nonlinear water wave simulator based on higher order spectral theory, in: Proc. 20th Int. Workshop on Water Waves and Floating Bodies, Longyearbayen, Norway.

[26] G. Ducrozet, Modélisation des processus non-linéires de génération et de propagation d'états de mer par une approche spectrale, Ph.D. Thesis, Ecole Centrale de Nantes, 2007 (in French).

[27] C. Canuto, M. Hussaini, A. Quarteroni, T. Zang, Spectral Methods in Fluid Dynamics, in: Springer Series in Comp. Phys., Springer, 1986.

[28] F. Bonnefoy, D. Le Touzé, P. Ferrant, Using a nonlinear spectral model for preparing three-dimensional wave experiments, in: Proc. 23rd Int. Conf. on Offshore Mech. and Arctic Engng., Vancouver, British Columbia, Canada.
[29] M. Benoît, C. Teisson, Laboratory comparison of directional wave measurement systems and analysis techniques, in: Proc. of the 24th Int. Conf. on Coastal Engng., ASCE, Kobe, Japan, 1994, pp. 42–56.
[30] T. Baldock, C. Swan, P. Taylor, A laboratory study of nonlinear surface waves on water, Philos. Trans. R. Soc. Lond. Ser. A Math. Phys. Eng. Sci. 354 (1996) 649–676.
[31] B. Molin, Hydrodynamique des structures offshore, Editions Technip, 2002, (in French).
[32] R. Dean, R. Dalrymple, Coastal Processes with Engineering Applications, Cambridge University Press, 2002.
[33] Y. Stassen, Simulation numérique d'un canal à houle bidimensionnel au troisième ordre d'approximation par une méthode intégrale, Ph.D. Thesis, Ecole Centrale de Nantes, 1999.
[34] W. Bateman, C. Swan, P. Taylor, On the calculation of the water particle kinematics arising in a directionnally-spread wavefield, J. Comput. Phys. 186 (2003) 70–92.
[35] F. Bonnefoy, Modélisation expérimentale et numérique des états de mer complexes, Ph.D. Thesis, École Centrale de Nantes, 2005 (in French).